Layer-oriented simulation tool

Carmelo Arcidiacono, Emiliano Diolaiti, Massimiliano Tordi, Roberto Ragazzoni, Jacopo Farinato, Elise Vernet, and Enrico Marchetti

The Layer-Oriented Simulation Tool (LOST) is a numerical simulation code developed for analysis of the performance of multiconjugate adaptive optics modules following a layer-oriented approach. The LOST code computes the atmospheric layers in terms of phase screens and then propagates the phase delays introduced in the natural guide stars' wave fronts by using geometrical optics approximations. These wave fronts are combined in an optical or numerical way, including the effects of wave-front sensors on measurements in terms of phase noise. The LOST code is described, and two applications to layer-oriented modules are briefly presented. We have focus on the Multiconjugate adaptive optics demonstrator to be mounted upon the Very Large Telescope and on the Near-IR–Visible Adaptive Interferometer for Astronomy (NIRVANA) interferometric system to be installed on the combined focus of the Large Binocular Telescope.

OCIS codes: 010.0010, 010.1080.

1. Introduction

Use of concept of multiconjugate adaptive optics[1–3] (MCAO) to overcome the limit of the small corrected field of view (FoV) that is achievable with classic adaptive optics[4] has been proposed. In adaptive optics (AO) a single reference star is used to measure the phase delay introduced by the atmospheric column located between the telescope and the star. Phase measurements are then used to drive a deformable mirror (DM) to correct the incoming wave front. In MCAO the goal is to reconstruct the three-dimensional structure of the turbulence over a FoV of several minutes of arc instead of in the single direction defined by the AO reference. To achieve this result a constellation of reference stars is sensed by several wave-front sensors (WFSs), and a few DMs are conjugated to turbulent atmospheric layers at different altitudes. Each DM corrects the turbulence of the conjugated part of the atmosphere by applying the information retrieved from the WFS measurements. A subject of some debate is the way to combine the signals coming from the reference stars or, in other words, the way to perform the wave-front-sensing operation. Of several possible solutions, two approaches are going to be implemented in several MCAO instruments in the near future: the star-oriented (SO) approach and the layer-oriented[5,6] (LO) approach. In the SO approach every detector is looking at a single reference, in this way allowing a three-dimensional reconstruction of the distorted wave front to be made; the correction is then applied to a certain number of DMs. In the LO approach the detectors are conjugated to some suitable altitudes, and they are looking at several stars; the wave fronts thus retrieved are then applied to DMs that are optically conjugated to the same altitudes as the relative detectors.

It is clear that, apart from possible tricks,[7] in the LO approach the number of detectors depends on the number of DMs used in the system rather than on the number of references, as it does in the SO approach. Another difference is that in the LO approach the light coming from the different references is normally optically coadded such as to take advantage of even faint references and to increase the signal-to-noise ratio (SNR) of the detectors. This implies the use of a pupil plane WFS, and the pyramid sensor[8] appears to be a good choice because of its high sensitivity.[9–11] The LO WFS splits the light of

C. Arcidiacono (carmelo@arcetri.astro.it) is with the Department of Astronomy and Space Science, University of Florence, Largo Enrico Fermi 5, I-50125 Florence, Italy. E. Diolaiti and M. Tordi are with the Department of Astronomy, University of Padova, Vicolo dell'Osservatorio 3, I-35132 Padua, Italy. R. Ragazzoni, J. Farinato, and E. Vernet are with the Istituto Nazionale di Astrofisica, Astrophysical Observatory of Arcetri, Largo Enrico Fermi, 5, I-50125 Florence, Italy. E. Marchetti is with the European Southern Observatory, Karl-Schwarzschild-Strasse, 2, D-85748 Garching bei Munchen, Germany.

Received 27 October 2003; revised manuscript received 3 May 2004; accepted 10 May 2004.

0003-6935/04/224288-15$15.00/0

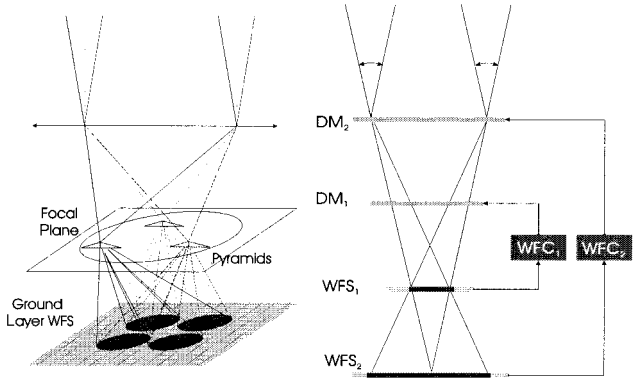

Fig. 1. Left, LO ground layer. The detector collects the beams coming from three NGSs split into four pupils by the pyramids. For the ground layer all the NGS split footprints overlap perfectly. Right, LO approach for two conjugation planes. There is one WFS, one DM, and one WFC for each loop. Subscript 1, upper conjugated plane; 2, ground conjugated plane.

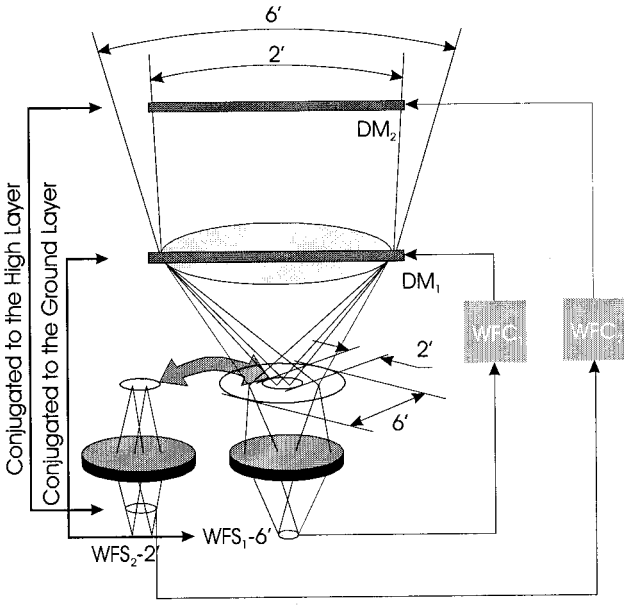

Fig. 2. MFoV layout: DM_1 and DM_2 are the deformable mirrors conjugated to the ground and to the high layer, respectively. DM_1 is driven by the stars lying in the annular 6-arc-min FoV only; DM_2, by the NGS in the central 2-arc-min FoV.

each reference star into four beams by means of pyramids located on an intermediate focal plane. Each of these beams produces a pupil image on a detector (normally a CCD; Fig. 1) that senses the different amounts of illumination of the four pupils. The intensity measurements allow one to compute the derivative of the wave front and finally to reconstruct the phase delay introduced by the perturbed layers. Of course the aberrations introduced by the layers near the detector's conjugation altitude are measured with more accuracy than those introduced by layers far away, which are smoothed out more as the distance from the plane increases.[12] Each detector–DM loop is hardware independent from the others (even if it is optically related), and this property allows one to tune the spatial–temporal parameters, such as the integration time on the WFS and the subaperture size on the detector (for instance, by binning the pixels on the CCD in different ways), to the statistical characteristics of the conjugated layers.

In all the SO approaches to MCAO the faint natural guide stars (NGSs; magnitude 17 and higher) present a low SNR, and they are not valid references for wave-front sensing. But in LO systems the optical coaddition of light allows one to take advantage also of starlight with a sufficiently high SNR. In principle, the same results can be obtained by use of a wave-front-sensing CCD camera with readout noise (RON) close to zero and the numerical coaddition of the various reference signals, even if a larger number of CCDs is needed in the optical approach because each reference is coupled with a phase sensor. However, the numerical approach is strongly dependent on the future availability of CCDs with these characteristics.

In a LO system the shapes of the footprints on detectors conjugated to different altitudes depend on the stars' positions with respect to the center of the FoV and on the conjugation altitude. A metapupil at a conjugate altitude is defined by the projection of the FoV onto this conjugated plane; in other words, it is the projection onto the conjugate plane of the DM. In a ground-conjugated WFS the pupils of different references overlap perfectly on the metapupil because the projection of the FoV, in this case, corresponds to the entrance aperture of the telescope. This means that every reference starlight senses the atmosphere on the ground layer independently of whether its position with respect to the FoV is taken into account for correction. In this way it is possible to consider for this loop a FoV that is larger than the scientific FoV, thus increasing the number of possible reference stars and of course the sky coverage. This kind of concept, in which different fields of view are considered, is called multiple field of view (MFoV) layer oriented.[13] For example, for a ground-conjugated detector an annular sky region about the corrected FoV is normally considered for the ground WFS, and in this way the light of the references inside the central FoV can be used by a detector conjugated to a higher altitude to drive the corresponding DM. In this way, splitting of the light among detectors can be avoided (see Fig. 2 and 3). To perform error budget analysis in LOST are implemented the possibility to introduce different sources of phase error as the misregistration of the couples DM-WFS as in conjugation altitudes as in position with respect of the metapupils. To compute the control matrix, the user can choose to use the simulated measurements of mirror modes with an arbitrary level of SNR, instead of the theoretical mirror modes. Other sources, such as those related to chromatism effects, are not taken into account.

The LO and MFoV techniques have one consider-

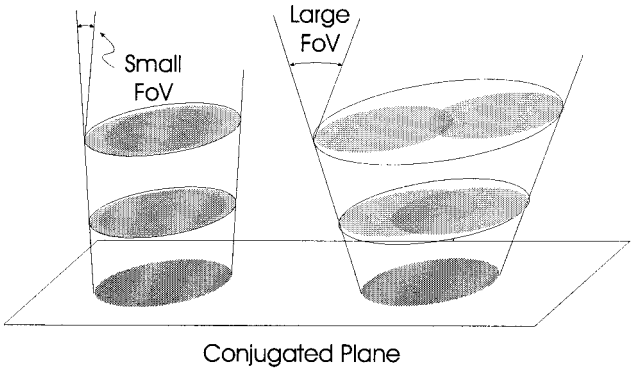

Fig. 3. Two FoVs, both relative to the ground. The superposition of the footprints on the nonconjugated plane decreases with distance from the conjugated plane: This shift produces a blur of frequency lower on the nonconjugated planes. Thus they are seen smoothed on the WFS. This effect depends on the separation angle between the references, and it is larger for large FoVs than for small FoVs.

able advantage in terms of real-time computing power compared with SO systems. In fact, as was already mentioned, the loops are hardware independent and the amount of information retrieved by the WFSs is essentially much less, i.e., only what is needed to drive the corresponding DMs. This results in a need for less CPU time and memory also for simulations related to these systems compared with simulations of systems based on the SO approach. This fact is relevant especially for extremely large telescopes (ELTs), (which, however, are not studied here), and in fact we emphasize that the complete simulations related to ELTs published so far are somehow related to the LO approach[14] or to use of a multigrid solver for the SO approach that is similar to the LO scheme in terms of atmospheric layer decoupling.[15]

The first version of the code, then called a layer-oriented simulation tool (LOST), was developed to introduce the LO approach. That first version was upgraded[16] to analyze the performance of the LO wave-front sensor arm of the Multiconjugate Adaptive optics Demonstrator[17] (MAD) and, finally, of a layer-oriented multiple field of view interferometric system[18] that comprises a Large Binocular Telescope (LBT) Interferometric Camera (LINC) and the Near-IR/Visible Adaptive Interferometer for Astronomy (NIRVANA) for the LBT.

In this paper, in Section 2 we describe in detail the LOST package and then in Section 3 present the main tests done to validate it. Several simulations results are presented in Section 4 for two specific cases.

2. LOST Simulation Package

The LOST code was developed in the Interactive Data Language version 5.2, and runs on Unix–Linux or Windows platforms. A typical simulation test takes few hours and several hundred megabytes of memory on a PC or a workstation with a 1–2-GHz processor, according to the required precision and the number and dimensions of the phase screens used to simulate the atmosphere.

One defines the system by writing a script file. In this way it is possible to set the main parameters of the telescope and of the AO system (such as diameter, the central obstruction, wavelengths, number of DMs, and the wave-front sensing and reconstruction methods). Two WFS noise models are implemented in the LOST code: the Shack–Hartmann and the pyramid wave-front sensors, and in both cases it is possible to set the characteristics of the detector that is used and the information about the geometry of the WFS. The parameters related to the DMs and WFSs can be different for each conjugation loop, exploiting the LO approach's ability to tune these quantities according to the statistical features of the conjugated plane. A block diagram of the LOST code is shown in Fig. 4. It has three main steps: the input definition, the main loop, and the output computation. The main loop is composed of a succession of actions executed sequentially and of two condition points in which the code compares the actual step to the integration timer or to the overall simulation timer. With the LOST code it is possible to analyze widely different AO systems: from single-reference AO by setting only one DM conjugated to the ground (or to another layer) and to one on-axis NGS, to the more-complex MCAO system that defines different DMs at different conjugation altitudes. The code is based on the geometrical projection of the NGSs footprints onto several layers and onto the DMs. The turbulent layers are represented as phase screens, and they are shifted during the simulation according to the wind-speed profile, assuming a Taylor hypothesis about the turbulence evolution. The NGS's asterism can be set by the user or randomly generated, assuming the distribution defined by the star galaxy luminosity function of Bahcall and Soneira[19] and according to the galactic latitude and longitude considered. The system's performance is expressed in terms of evolution of the Strehl ratio (SR) and of the point-spread function (PSF), both computed for each time evolution step. The PSFs are integrated during the simulation to generate a long-exposure SR map. The LOST code evaluates these quantities for one or several sky directions inside and outside the FoV as well. An optical coaddition of the NGS wave front for each loop is implemented; however, we consider the possibility of a numerical LO sensor only for the ground loop (using common CCDs or L3 CCDs[20]). The physical meaning of each simulation section in the block diagram description is discussed in what follows.

A. Generation of Atmospheric Layers

As in most AO simulation packages, in the LOST code each atmospheric phase screen is computed by a Fourier-transform technique in which the subharmonic frequencies[21] are added to match the Kolmogorov or the von Kármán power spectrum (the latter is characterized by outer scale L_0). In Fourier space a

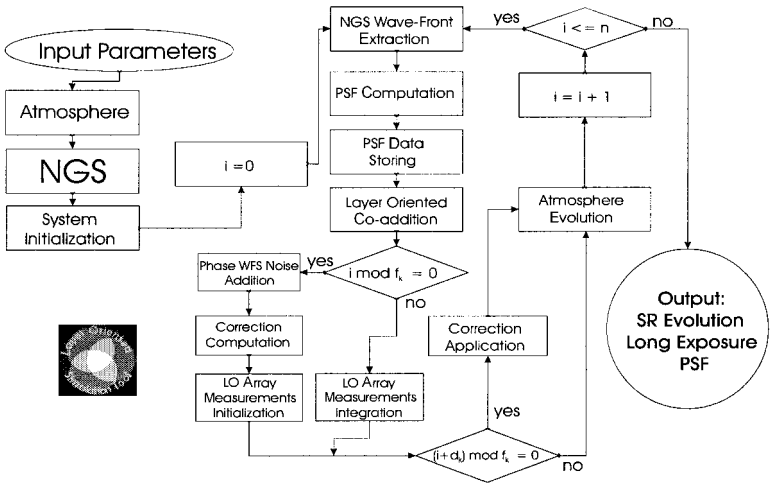

Fig. 4. Block diagram of the LOST code. The input parameters that define the characteristics of the atmosphere and the system are provided by filling a script text with the parameter values. This script indicates to the code whether the atmosphere, the stars, the mirror modes, or any other information about the telescope or the adaptive system has to be computed or loaded from existing files. Before the main MCAO loop all the constant quantities, such as the control matrix, are computed and the variables such as the PSF, are initialized. Here the main loop starts with the definition $i = 1$: First the wave fronts of the NGSs are retrieved as seen by the telescope and then the PSFs are computed for each direction in which the user wants to retrieve the SR. These PSFs are saved and integrated along the cycles of the loop. The NGSs' wave fronts are combined in the LO mode for each conjugation altitude. In this way the LO noise-free measurements are computed and integrated at each loop. The integration covers f_k cycles, where the subscript k refers to the relevant loop. The phase noise that is due to the WFS is then added to the LO measurements, and the correction is computed. Corrections are applied to the DMs at the same frequency as that used for the WFS, with the delay d_k that is due to the operations performed by the real-time computer and to other possible sources taken into account. The integration time values f_k are usually different for the different WFSs. At each iteration the phase screens are shifted according to the wind speed and direction, and finally iteration counter i is updated. When the last iteration, $i = n$, is reached the integrated PSFs, the SR evolution, and other required data, such as the mode coefficients and the residual wave-front error, are saved in the output files.

random value $0–2\pi$ of the phase is associated with each frequency (and, iteratively, with each screen). Finally, we normalize each phase screen to have, on average, the correct amount of phase variance in the pupil aperture according to the theoretical prediction.[22,23] In the Kolmogorov case our procedures generate the phase screens by using the power spectrum function, $\mathrm{PS}(r_0, k)$, defined by the Wiener relation

$$\mathrm{PS}(r_0, k) = 0.023 {r_0}^{-5/3} k^{-11/3}, \tag{1}$$

where r_0 is the Fried parameter and k is the spatial frequency. The von Kármán power spectrum is defined by

$$\mathrm{PS}(r_0, k) = 0.023 {r_0}^{-5/3} (k^2 + {k_0}^2)^{-11/6}, \tag{2}$$

where k_0 is the frequency that corresponds to the outer scale L_0. We normalize the arrays by dividing the phase screens by the square root of the average variance. We compute this value by averaging the phase's standard deviation relative to a square-grid telescope pupil over the phase screen. Then each screen is multiplied by a factor that is the theoretically predicted[22,23] phase variance over the pupil, ${\sigma_\varphi}^2$. For the Kolmogorov spectrum, ${\sigma_\varphi}^2$ is expressed by

$${\sigma_\varphi}^2 \approx 1.03 (D/r_0)^{5/3}, \tag{3}$$

whereas, in the von Kármán spectrum, ${\sigma_\varphi}^2$ is defined by

$${\sigma_\varphi}^2 \approx 0.09 (L_0/r_0)^{5/3}, \tag{4}$$

where r_0 is related to the Kolmogorov value by a more-complex relation.[23] We compute the phase screens by normalizing for the theoretical phase variance and using a fixed spectrum; then the average amplitude of each phase screen is determined.

The physical dimensions of the layers generated depend on the pixel size used. This size is defined as the ratio of the dimensions of the pupil diameter expressed by the user in pixel units and in meters. The lower limit for the pixel size should be the smallest r_0 taken into account for the various phase screens.

B. Loop

The basic clock is defined by phase screen evolution interval Δt. This user-defined parameter sets the lower temporal step of the simulation. Every other temporal parameter, such as the integration time of the wave-front sensors and the delay applied to the DM correction, must be an integer multiple of this number. One simulates the atmospheric evolution by shifting each phase screen by a displacement

$$\Delta \mathbf{s}_i = \mathbf{v}_{\mathrm{wind},\, i} \Delta t, \tag{5}$$

where $\mathbf{v}_{\mathrm{wind},\,i}$ is the speed vector of the ith layer. This shift is performed in an accurate way through the combination of a rigid shift of the screen matrix and a linear interpolation. To preserve the statistical layer characteristics we apply the shift at each step by starting from the original layer array rather then by reiterating the shift of the previously shifted screen. Otherwise, this procedure would introduce a smearing if it were applied several times.

The control algorithm is a pure integrator, but other filters can be implemented. For every temporal step the code computes the measured wave front of each NGS by coadding the portions of the phase screens illuminated by the guide stars and subtracting the previous computed DM correction:

$$\mathrm{WF}_i(\mathbf{x}) = \sum_{j=1}^{n\mathrm{layer}} L_j(\mathbf{x} - h_j\theta_i) - \sum_{k=1}^{n\mathrm{DM}} \mathrm{DM}_k(\mathbf{x} - h_k\theta_i), \tag{6}$$

where L_j is the jth layer, DM_k is the kth DM, $\mathbf{x}$ is a position vector on the pupil, θ_i are the off-axis coordinates of the ith star, h_k is the conjugation altitude of the kth DM, and h_j is the altitude of the jth layer. On each layer we define an x, y coordinate system with the origin in the center of the FoV to identify the off-axis angle and the position of each star. Now we are able to focus on the desired layer altitude according to the LO scheme. We superpose the NGS wave fronts, considering the positions of the footprints at the conjugation altitudes. Each star's wave front is weighted according to the related NGS intensities as shown in Eq. (7) below. The final result is an array that contains the phase measurements of the layers at the conjugation altitude:

$$M = \frac{\sum_{i=1}^{n\mathrm{star}} \mathrm{WF}_i(x_i, y_i) I_i}{\sum_{j=1}^{n\mathrm{star}} I_j}, \tag{7}$$

where M is the array that represents the weighted sum of the NGS wave fronts as seen focused on the conjugation altitude, WF_i is the ith NGS wave front, and I_j is the jth value of star intensity (in linear units). Of course, one must superpose WF_i by taking into account the position of the footprint at the conjugation altitude.

The integration time of the WFS has to be larger than an evolution time step of the atmosphere to simulate the blurring of the wave-front information that is due to the finite exposure time of the WFS.

These layer measurements are then used to compute the correction, and, after a number of steps equivalent to the time delay, the DMs are subtracted from the wave fronts of the NGSs. In a closed loop the reconstructed phase refers to the residual turbulence, and the corresponding correction is actually a differential correction.

The incoming phases combined in LO mode focused to the conjugation altitude are sampled with a resolution that is much better than that applied to the WFS measurements. To achieve the spatial sampling used, we spatially average the measurements to get a measurement relative to each WFS pixel (see Fig. 5). In the real system these WFS pixels can be read while they are assembled in squares to minimize WFS noise. In the simulator we also consider this possibility by averaging the phase values of a screen of pixels in a square that comprises the assembled pixels and finally associating them to the relative noise (see Subsection 2.C below).

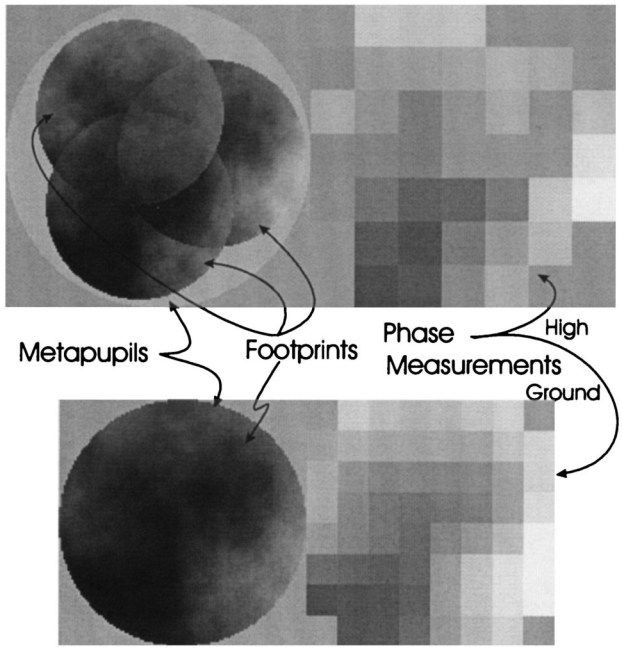

Fig. 5. Results of the LO procedure described in the text. Top, high-altitude WFS measurement: the footprints of three NGSs do not perfectly overlap because of their different positions in the FoV. Metapupils (the circles that define the projection of the FoV on the conjugated planes) are also shown. The real measurements are at the right, where the effects of the WFS spatial sampling (7×7 and 8×8, respectively, for high and ground WFSs) are visible. Bottom, measurements of the ground WFS. Here the pupil footprints and the metapupil overlap perfectly. For the two images we apply the same linear scale to show that the dimension of the highest metapupil is larger than the ground state metapupil.

Finally, features of the MFoV approach are implemented. In particular, we consider that the NGSs that lie in the external annular FoV are used to drive the ground layer wave-front sensor, whereas the stars of the central FoV are used to drive the higher DMs (see also Ref. 24).

C. Addition of Phase Noise

The LOST code implements the procedures to simulate the error in phase measurements relative to the SH WFS and the pyramid. In the latter case in the computation of the NGS photon flux the splitting of light among the various loops is taken into account (in the MFoV case this is done only for the central FoV reference stars). To simulate the WFS response we take into account all the sources of noise: Poissonian distribution of photons, RON, dark cur-

rent, and sky background. The LOST code computes the error that is due to the WFS directly in terms of phase for all the subapertures that compose the metapupil. In the SH case the LOST code applies the noise propagation equations in Ref. 25, which associates the noise relative to the intensity measurements with the noise relative to the measured phases. The noise that is due to each considered source is given in terms of variance in a subaperture, $\sigma_\varphi{}^2$, expressed in square radians:

$$\sigma_{\varphi,\mathrm{photon}}{}^2 = \frac{\pi^2}{2}\frac{1}{n_{\mathrm{ph}}}\left(\frac{N_T}{N_D}\right)^2, \tag{8}$$

$$\sigma_{\varphi,\mathrm{RON+dark}}{}^2 = \frac{\pi^2}{3}\frac{\sigma_e{}^2}{n_{\mathrm{ph}}{}^2}\left(\frac{N_S{}^2}{N_D}\right)^2, \tag{9}$$

$$\sigma_{\varphi,\mathrm{sky}}{}^2 = \frac{\pi^2}{3}\frac{n_{\mathrm{bg}}}{n_{\mathrm{ph}}{}^2}\left(\frac{N_S}{N_D}\right)^2, \tag{10}$$

where n_{ph} is the number of photons detected in the subaperture, $N_S{}^2$ is the total number of WFS pixels per subaperture, and N_T is the image's FWHM. This FWHM is equal approximately to the ratio λ/r_0, where λ is the wave-front-sensing wavelength, if r_0 is larger than the dimension of the subaperture, d, whereas N_D is the FWHM in pixels of the diffraction pattern of the subaperture, $N_D \propto \lambda/d$. n_{bg} is the number of photons detected in the subaperture that come from the sky background. σ_e is the root mean square, in photoelectrons, that is due to RON and dark counts:

$$\sigma_e = (\sigma_{e,\mathrm{RON}}{}^2 + N_{e,\mathrm{dark}})^{1/2}, \tag{11}$$

where $\sigma_{e,\mathrm{RON}}$ is the root mean square that is due to the RON (equal to the RON value) and $N_{e,\mathrm{dark}}$ are the dark counts. Applying Eq. (11), we obtain an array of variance values (for each subaperture) of the same dimensions of the array that represent the phase measurements. This variance array permits the computation of random phase noise maps: By multiplying this array point by point by a random array of unitary variances, one can retrieve the noise array. An array of random numbers is generated for each phase measurement. This noise is added algebraically to the measurements given by the LO procedure before the measurements are used for the fit with the Zernike polynomials. In the WFSs conjugated to the high-altitude layers the footprints of the stars do not completely overlap, and illumination of the subapertures depends on the positions and magnitudes of the references. This dependence affects the phase noise variance array, which is not uniform in that it has valleys where the footprints overlap and peaks onto which only the light of a few faint NGSs is projected. The model of the pyramid WFS in the simulator is based on geometrical approximations and on the WFS noise theory developed for the SH sensor. We assume, in an operative sense, that each SH subaperture corresponds to the four WFS pixels used to sample the image of the four pupils reimaged by the pyramid. Under this assumption the pyramid is quite equivalent to a quad-cell SH sensor: the four pixels of the quad cell correspond to the same pixels on the four pupils of the pyramid. These four pixels, one for each pupil, permit measurement of the phase in a single subaperture of the main pupil (see Fig. 6). The LOST code uses a pure integrator control law, and the wave-front reconstructor is not noise weighted. The code applies the same gain to all the mirror modes computed, relative to each DM. To cut the noisier modes, the user has to set a high condition number (the standard value applied is 10) for the cut of the eigenvalues in the computation of the inverse of the interaction matrix (see Subsection 2.D below). In this way is possible to manage measurements in the proper way when the SNR is low.

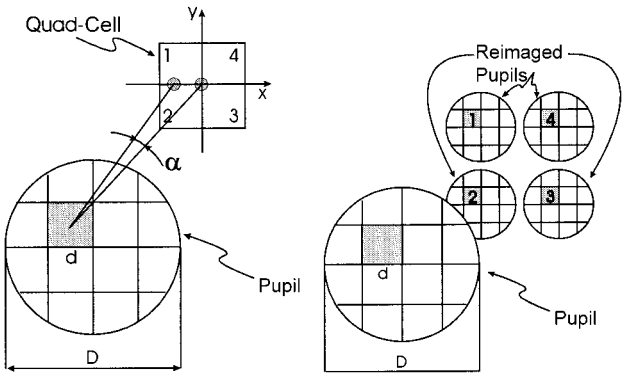

Fig. 6. Analogy between the quad-cell SH (left) and the pyramid WFS (right). D, dimension of the metapupil; d, dimension of the subaperture. In both cases, the light collected by a single subaperture is measured by four pixels: the quad cell in the SH case and the four corresponding pixels on the four reimaged pupils in the pyramid case. In the SH sensor we measure shift α of the spot, whereas in the pyramid we compute the intensities of the four pixels to retrieve the wave-front derivatives.

To simulate the effect of a pyramid-based WFS we consider the SH procedure described above, assuming a modulation of the pyramid that always gives a linear response of this device for every degree of correction. We model the coefficients N_S, N_D, and N_T to be consistent with the characteristics of the pyramid WFS, and we substitute these values into Eq. (8)–(10).

Several studies[9,26] predicted a gain in terms of limiting magnitude of the pyramid with respect to the SH sensor; anyway, we chose a conservative approach in which this advantage is not considered. From the comparison with the quad cell, the number of pixels $N_S{}^2$ used to sense the wave front in each subaperture is 4. N_D in the SH sensor is the dimension in pixels of the PSF pattern of a diffraction-limited spot for a subaperture d. Instead, the LOST code uses for a pyramid the linear dimension of the quad cell itself, expressed in pixels ($N_D = 2$). The pyramid is a pupil plane WFS, and there is no NGS spot (as there is in the SH sensor) on the 4 pixels that compose the quad cell, but they are completely illuminated by a portion of the pupil image (except those

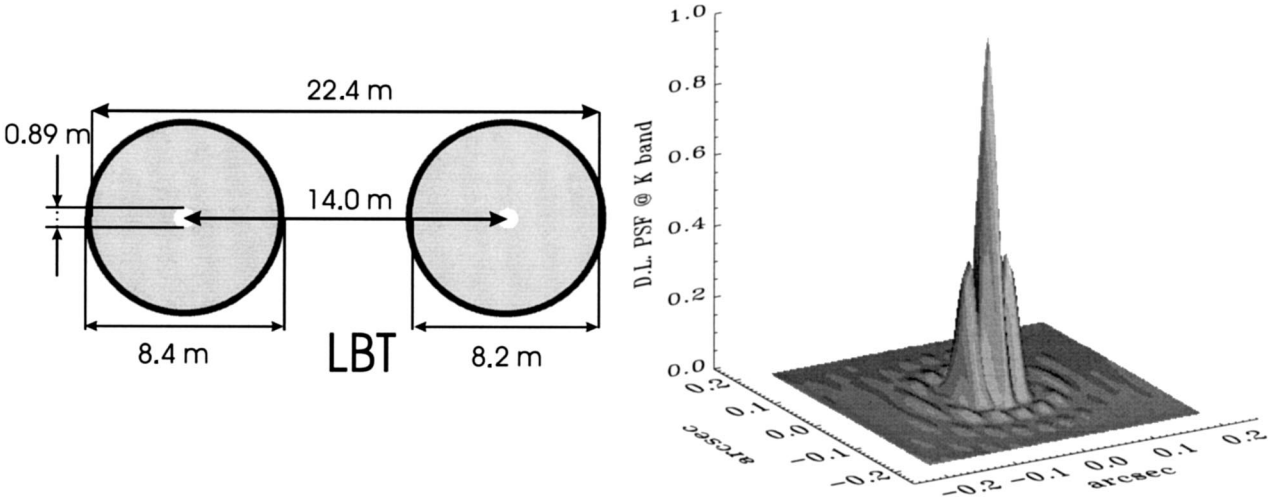

Fig. 7. Left, twin primary mirrors geometry of the LBT. The primary mirror diameter is 8.4 m. The entrance pupil is due to the secondary mirror and is only 8.2 m. Right, diffraction-limited PSF in the interferometric case in the K band as seen by the LBT and computed with the LOST.

at the border of the metapupil). So for a pyramid we can assume that the dimension in pixels of the illuminated portion of the quad cell is the side of the quad cell itself. If we refer to the variance of a single subaperture, Eq. (9) becomes, for dark current and RON,

$$\sigma_{\varphi,\mathrm{RON+dark}}{}^2 = \frac{4\pi^2}{3}\left(\frac{\sigma_e}{n_{\mathrm{ph}}}\right)^2. \tag{12}$$

The N_T parameter is present only in the Eq. (8) (relative to the photon noise) and its value is computed at every step of the loop on the instantaneous PSF by use of the Fourier transform. One finds the sky background noise by substituting the parameters found for the pyramid WFS:

$$\sigma_{\varphi,\mathrm{sky}}{}^2 = \frac{\pi^2}{3}\frac{n_{\mathrm{bg}}}{n_{\mathrm{ph}}{}^2}. \tag{13}$$

D. Zonal and Modal Reconstruction and Correction

The user can choose either a zonal or a modal method with which to compute the shapes of the DMs. The measurements computed with the simulated phase sensors are the input data of the reconstruction-correction procedure. These are expressed in arrays of phase values, where the number of arrays is equal to the number of WFSs. There is a one-to-one correspondence between the elements of the arrays and the measurements that come from the assembled pixels (which we also call subapertures). But not all the subaperture measurements are used in the reconstruction procedure. Several subapertures can be only partially illuminated by the stars' footprints or not at all. The code uses in the reconstruction only those subapertures illuminated at least for a user-defined fraction (the standard is 10%), even if the computation of the DM surfaces is performed over all the metapupils.

In a zonal reconstruction the DM is computed by linear spline interpolation of the phase noise measurements retrieved by the WFS. But usually one analyzes the performance by taking into account modal reconstruction. In modal reconstruction the measurements are fitted with a user-defined number of Zernike polynomials or set of modes (such as Karhunen–Loeve or user-defined modes or, for instance, the measured mirror modes). This fit is performed by inverse matrix operation: for each loop l we solve the system that relates the LO phase noise measurements array $\tilde{\mathbf{M}}_l$ to DM modes $\mathbf{Z}_l$ and obtain as a result the coefficient vector $\mathbf{c}_l$ relative to each mirror mode considered:

$$\mathbf{c}_l = \mathbf{I}_l{}^{+}\tilde{M}_l, \tag{14}$$

where $\mathbf{I}^{+}$ is the inverse of the interaction matrix computed by singular-value decomposition. As in the real LO systems this matrix is computed once for each NGS asterism. We assume that the DMs are able to produce the modes $\mathbf{Z}$ used to fit the measurements, and we compute the DMs as linear combinations of $\mathbf{Z}$. For each loop we take into account a gain coefficient, g_l, such that the mirror mode coefficient $\mathbf{a}_{n+1,l}$ applied to each DM_l is defined by

$$\mathbf{a}_{n+1,l} = \mathbf{a}_{n,l} + g_l\mathbf{c}_{n+1,l}, \tag{15}$$

where the subscripts n and $n + 1$ refer to two consecutive steps of the same loop. The maximum number of modes that is useful for reconstructing the phase measurements is related to the number of subapertures considered. One selects the modes by keeping only the polynomials with associated singular values larger than a condition number (usually defined as the 10% of the largest eigenvalue) to ensure greater stability of the correction-rejecting unstable modes.

Table 1. SR for Two Kinds of Noise: Photon Noise and RON, and Photon Noise Only[a]

M_R	WFS Sampling	Gain	RON	Integration Time (s)	Rigaut SR[b]	LOST SR
14.83	10×10	0.683	5.0	0.011	0.5	0.46 ± 0.02
15.81	14×14	0.400	0.0	0.004	0.5	0.53 ± 0.02

[a]Computed for the parameters in Ref. 31. The SR is compared in columns 6 and 7 to that given in Ref. 31, and the two are approximately the same. The error values are the standard deviations of the instantaneous SR contribution to the long-exposure SR computed during the simulation.
[b]Ref. 31.

E. Interferometry

We implemented interferometric features to simulate the LBT telescope with two independent 8-m-class telescopes on the same mount (Fig. 7). The two systems run in parallel, using the same parameters but each looking to its own portion of the same layers. We collected the two wave fronts of each test star in a single array (according to the specific dimension of the LBT) and used them to compute the interferometric PSF of the stars by performing a Fourier transform. As in the single-channel case, after a number of iterations defined by the user the long-exposure PSFs start to be integrated as the PSFs that were computed for all the steps of the simulation are collected. These instantaneous PSFs are used also to compute the instantaneous interferometric SR (defined as the ratio of the central value of the computed PSF to the PSF in the diffraction-limited case). However, more interferometric properties will be obtained by development of the code specifically to ensure more-accurate and -realistic results, including detailed behavior of the fringe tracker[27] (an issue that, however, is not discussed in this paper). The LOST code at present assumes that the piston term between the two arms is corrected by the system, except for small, random errors.

F. Simulation Outputs

For every temporal step the residual wave fronts are used for computing the instantaneous PSF in all the sky directions defined by the user. The SR is evaluated as the ratio between the center of these PSFs and the same value relative to the diffraction-limited case for each iteration. We coadd the PSFs step by step for each direction to retrieve, at the end of the simulation, the long-exposure PSFs relative to the temporal interval over which the coaddition was set by the user. Finally, the code saves the instantaneous SR data and the integrated PSFs and computes the long-exposure SR map over the FoV by linearly interpolating the SR value of each sky direction. In this way the user is able to compute the SR and the PSF for the directions previously set.

3. Validation of the Code

A. Comparison with Theory

We performed several tests to check the validity of the LOST simulations. The phase screens simulated the same properties predicted theoretically for Kolmogorov turbulence as well as the isoplanatic patch size angle and the temporal error fit that were theoretically predicted.[28] We also checked the relationship between phase variance σ_ϕ and the wavelength[28] and whether the distribution of the residual σ_ϕ with respect to the Zernike fitted modes fitted the distribution predicted.[22] We tested the influence of fitting error in the zonal case and the influence of the number of Zernike polynomials used in the modal correction on achievable performance. In all these cases we took into account an on-axis single-reference system without considering the effects of noise caused by the WFS on the phase measurements. We repeated each test several times with different randomly generated phase screens to compare the distribution of the LOST code results with the theoretical expectations. All the tests performed yielded results that were in agreement with the theory: The difference between the LOST results and the theoretical values was less than 10%, as was also reported in Refs. 29 and 30.

B. Shack–Hartmann Test

We simulate the SH WFS by using Eqs. (8)–(10) to compute the phase noise associated with WFS measurements. We validated our procedures by comparing the LOST code results with the cross-check results published in Ref. 31. Here the results of three simulation codes are presented and their performance compared. The three results refer to a specific system in specific atmospheric conditions and use the same simulation parameters. We followed the same strategy to check our code. In several simulations under the same conditions we found results in good agreement (see Table 1 and Fig. 8).

C. Pyramid Test

We cross checked our model for the noise of the pyramid WFS, comparing our simulations with similar simulations performed by with the numerical code CAOS.[32] The MAD system was simulated with both LOST and CAOS packages.[24] For MCAO the WFS sensor was a pyramid, and no modulation was considered. If we assume an optimistic value of $r_0 = 0.18$ m at the V band (0.5 μm), the two codes give similar results, with a peak SR of approximately 50% and an average SR of 38% computed on the guide star (the SR includes tilt). For details of the system parameter that we used, see the Subsection 4.A below. The CAOS simulation package uses an end-to-end

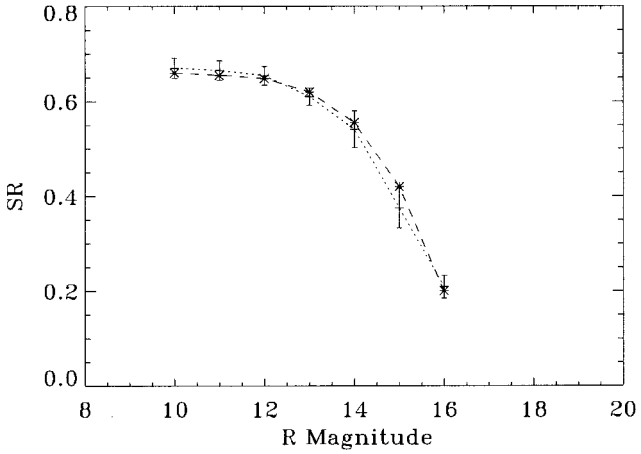

Fig. 8. Dashed curve, data of Rigaut *et al.*[31]; LOST results are represented by the dotted curve. Both curves refer to the Gemini telescope and the classic AO case with one DM conjugated to the ground layer, $r_{0,V} = 0.25$, $r_{0,H} = 0.90$, σ_e of 5 e^- per pixel per frame, 10×10 sampling, and a zonal DM reconstruction. $\Delta\lambda = 0.22$ (μm) bandwidth; overall quantum efficiency, 0.5; scientific and wave-front sensing wavelengths, respectively, $\lambda_{sc} = 1.6$ (μm H band) and $\lambda_{WFS} = 0.7$ (μm R band); diameter, 7.9 m; and central obstruction, 1.2 m. Data relative to our simulations were obtained with 1-s exposure. Curves were obtained after optimization of the two free-parameter gain and integration times of the WFS. Error bars, standard deviations of the instantaneous SR contribution to the long-exposure SR computed during the simulations.

model of a pyramid WFS, whereas the LOST code uses the relations derived for the SH WFS. However, our simulations agree with these simulations because the case considered belongs to the bright regime of integrated magnitude where the pyramid gain[9,26] with respect to the SH sensor is negligible. We also compare our results with those obtained by Fedrigo *et al.*[14] and with those that are relative to the MAD. Again, the results of the two codes are in good agreement, as listed in Table 2.

4. Applications

The LOST software was developed to simulate a generic layer-oriented wave-front sensor system. In what follows, we present four different results relative to the MAD and NIRVANA MCAO LO systems.

Table 2. Comparison of LOST MAD Simulations and the Simulation Described in Ref. 14[a]

Integrated Magnitude	LOST SR Results	SR Results from Ref. 14
9	22 ± 5	25 ± 2
10	21 ± 5	24 ± 2
11	18 ± 4	20 ± 2
12	10 ± 2	11 ± 1
13	3 ± 1	2 ± 1

[a]The same eight-star asterism over a 2-arc-sec FoV is assumed in both cases, as is an identical atmospheric model characterized by an overall $r_0 = 0.83$ m at the K band and the Kolmogorov power spectrum.

Table 3. Atmospheric Parameters Used in the Simulations[a]

Layer	Altitude (m)	r_0 at K (m)	Wind (m/s)
1	0	1.08	6.6
2	1800	3.79	12.4
3	3200	3.00	8.0
4	5800	6.25	33.7
5	7400	7.62	23.2
6	13000	3.79	22.2
7	15800	10.39	8.0

[a]For each layer an outer scale of 20 m is assumed. r_0 was computed for the K band.

In both cases we considered a seven-layer atmosphere with the typical conditions measured at Cerro Paranal (Chile), characterized by an average seeing value at the V band of 0.73 arc sec, equivalent to an overall $r_{0,V} = 0.14$ m. In both cases the results are computed at the K band, $\lambda = 2.2$ μm, with a corresponding $r_{0,K}$ of 0.83 m. The MAD simulations are performed with an existing set of phase screens (Table 3), whereas the atmosphere relative to the NIRVANA system is computed by the LOST code.

To measure the value of the SR over the 2-arc min FoV, for the MAD we use a constellation of sky directions, whereas for NIRVANA we consider a simple square grid (Fig. 9).

A. LO Wave-Front Sensor for MAD

The MAD module will be mounted at the visitor Nasmyth focus of UT3, an 8-m-diameter telescope of the Very Large Telescope. The layer-oriented wave-front sensor of the instrument is currently installed at the Astrophysical Observatory of Arcetri, the SH WFS, the main optical train, and a real-time computer are located at the European Southern Observatory at Garching, Germany, and the CAMCAO infrared camera is located in Lisbon (see also Ref. 33).

The capabilities of the MAD layer-oriented wave-front sensor (for specifications used see Tables 4 and 5) can be analyzed numerically with good accuracy by the LOST code. Two sets of DM modes are used, one for each conjugation altitude; each set contains the 59 closest modes to the 59 first Zernike polynomials that a DM can generate. In the following simulations a zenith angle of 30° was assumed.

The values of the integration time used in the simulations are selected by an optimization test. By running an automatic interactive data language procedure, we use all the possible combinations of integration times of the two WFSs (ground and high) in short simulations of 1 s in which only the SR on the center of the field is computed. In this way the best values for these parameters are retrieved for both cases considered below. Also, the gains used in the simulations are chosen through short simulations; in particular, we considered a grid of gain values (from 0.4 to 0.9, with 0.1 spacing between consecutive loops) applied to the loops by use of the best integration times.

We analyzed two real star asterisms on a 2-arc min

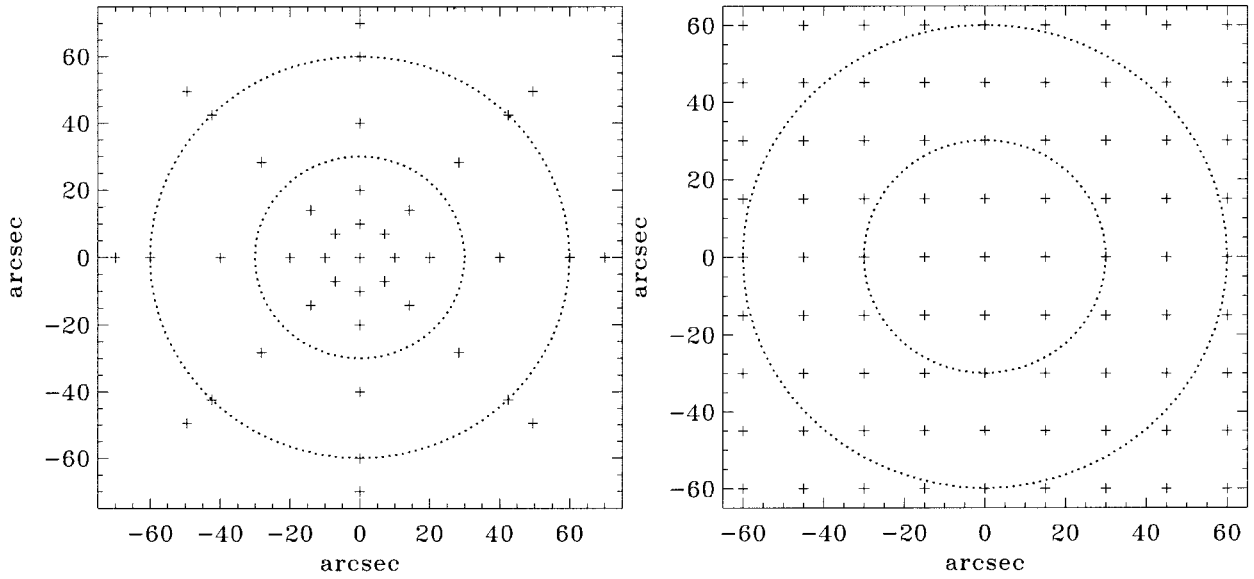

Fig. 9. Left, each cross indicates a direction where the SR is computed in the MAD case; these coordinates are defined by the user. Right, each cross indicates a direction where the SR is computed in the NIRVANA case; these directions are positioned on a square grid and were generated by the LOST code. In both cases the two circles have 1- and 2-arc-min diameters. The origin corresponds to the on-axis direction.

FoV with six and eight stars, respectively. The six-star asterism right ascension was centered in 16 h 25 min 17.7 s and dec $\delta - 40°39'53''$ of galactic latitude l 5.5° with $V = 9.85$ integrated magnitude (Fig. 10), whereas the eight stars were centered in RA 10 h 35 m 50.1 s and dec $-58°12'50''$ of galactic latitude 0° with V = 5.03 integrated magnitude (Fig. 11). These are bright stars, and to obtain more-interesting ones we shifted the integrated magnitude to the 14th. Assuming a maximum difference in star brightness of 3.5 magnitude and a minimum separation of stars of 20 arc sec, the probability of finding a suitable star asterism brighter than magnitude 14 integrated on a 2-arc-min FoV is 70% for a galactic plane and 3% for the galactic poles.[34] Figures 10 and 11 summarize the results. Even if the integrated magnitude of the two cases is equal, the SR is more nearly uniform for the six stars than for the eight stars because the difference in brightness between the references is larger in the latter one: The average SRs over the 2-arc-min FoV are 0.21 and 0.17 for the six and the eight stars, respectively, whereas the peak SRs are 0.29 and 0.28.

B. NIRVANA

The LBT has two $D = 8.4$ m primary mirrors mounted upon a common altitude-azimuth mounting, with a center-to-center distance of 14.4 m.[35] The two channels are symmetrical and are supplied with twin adaptive secondary units.[36] Whereas the first-generation instruments[37–40] are close to the integration phase, the second-generation instruments are in the design phase, as is LINC–NIRVANA.[18] The LINC module will combine the two LBT channels to use the natural 22.8-m baseline given by the edge-to-edge distance of the two primary mirrors. To

Table 4. Common Simulation Parameters Considered for the MAD[a]

D (m)	FoV (arc min)	λ_{science} (μm)	λ_{WFS} (μm)	$\Delta\lambda_{\text{WFS}}$ (μm)	$M_{R,\text{sky}}$	Exposure Time (s)	Overall Quantum Efficiency	Delay Time (ms)
8	2	2.2	0.55	0.4	20.0	1.0	0.2	2.5

[a]The pixel size of the phase screens is always 0.07 m/pixel, with a diameter of 112 pixels. The overall quantum efficiency, 0.2, gives a flux of 5.36×10^{11} photons/s at $\lambda = 0.55$ μm wavelength ($\Delta\lambda = 0.4$ μm bandwidth) and for a star of magnitude $V = 0$.

Table 5. Common Simulation Parameters Used in the MAD Simulations

DM	Altitude (km)	Gain	WFS Sampling	Integration Time (ms)	RON (rms)	Dark	Zernike Modes
1	0	0.6	8×8	5.0	4.5 e^-/pixels/frame	500 e^-/pixels/s	59
2	8.5	0.6	7×7	10.0	3.5 e^-/pixels/frame	500 e^-/pixels/s	36–43

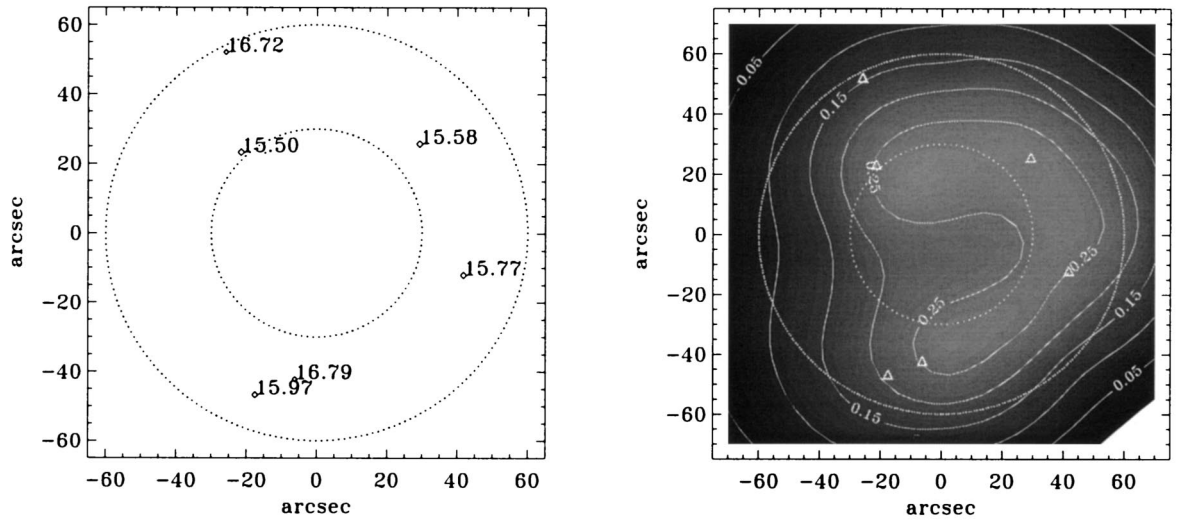

Fig. 10. Six-star asterism for the MAD case. Left, reference guide stars' positions and magnitudes are indicated by diamonds. Right, long-exposure SR map in the *K* band. The guide stars' positions are marked by triangles. In both figures the two circles have 1- and 2-arc-min diameters. The origin corresponds to the on-axis direction.

achieve this result, one needs an high level of wavefront correction. In a first phase the LINC instrument will work by using the single-reference AO correction provided by the secondary units only. In a second phase the correction will be enlarged to a square field of view of 20 arc sec × 20 arc sec. To achieve this goal requires a uniform correction, which is supplied by the MCAO NIRVANA instrument. The adaptive secondary units will perform the ground-layer correction; NIRVANA will provide a high-level correction over the 2-arc-min FoV with the addition of another DM per arm. Finally, the corrected wave fronts will be combined with the piston correction provided by the fringe tracking,[27] enabling

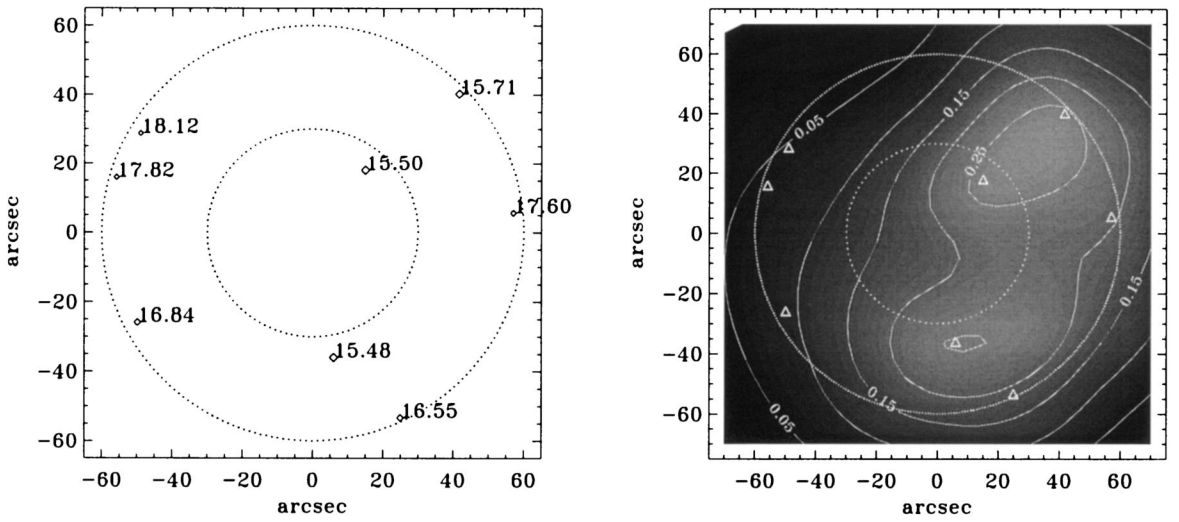

Fig. 11. Eight-star asterism for the MAD case. Right, positions and magnitudes of the reference guide stars. Left, long-exposure SR map in the *K* band. In both figures the two circles have 1- and 2-arc-min diameters. The origin corresponds to the on-axis direction.

Table 6. LINC–NIRVANA Common Simulation Parameters of Both Channels[a]

D (m)	FoV	$\lambda_{science}$ (μm)	λ_{WFS} (μm)	$\Delta\lambda_{WFS}$ (μm)	$M_{R,sky}$	Exposure Time (s)	Overall Quantum Efficiency	Delay Time
8.2	2′ and 6′	1.2 and 2.2	0.75	0.5	20.0	1.0	0.3	2 × integration time

[a]In the interferometric mode we consider the same parameters for both arms. In this case instead of the measured (mirror) modes of the DMs we use the Zernike polynomials, assuming that DMs are able to reproduce every Zernike polynomial.

Table 7. AO System Parameters Used in the NIRVANA Simulations[a]

DM	Altitude (km)	Gains	Integration Time (ms)	RON (rms)	Dark	Zernike Modes
1	0.1	0.55	8.0	3.5 e^-/pixels/frame	500 e^-/pixels/s	609
2	6	0.45	6.0	3.5 e^-/pixels/frame	500 e^-/pixels/s	324

[a]The binning factors used are 2 × 2 for the ground layer DM and 4 × 4 for the high DM.[41,42] In both cases the WFS sampling is 12 × 12.

the large-FoV interferometric focal station to be mounted with the other scientific instruments.

The NIRVANA module is composed of two MCAO channels that provide high layer correction. The MCAO system is driven by natural stars that lie within a 6-arc-min FoV. The NIRVANA module[18] is designed to use an optical or a numerical coaddition of the NGS light following the LO approach. In particular, to extend the FoV, and thus the sky coverage, when one is looking for the references, the MFoV technique is applied.[13] The capabilities of an instrument such as LINC–NIRVANA can be analyzed numerically with a good degree of accuracy with the LOST code (the system parameters used are listed in Table 6). The values of the spatial–temporal sampling of the WFS used in the simulations were computed through an automatic optimization procedure: A grid of the possible combinations of integration times and sampling of the two WFSs (ground and high) was used for short simulations of 0.3 s; only the SR on the NGS was computed. In this way the best values for these parameters were retrieved for each asterism, with the average SR assumed to be the figure of merit to be optimized. Also, the gains used in the simulation were evaluated by short simulations in which a grid of values (0.05–1.2, with 0.05 spacing) was checked by application of the best integration times retrieved. The conjugation altitudes used for the high DM were selected by a similar test.

We recall here that in the MFoV the ground loop is driven by use of references in a FoV that is larger than the corrected FoV. The secondary adaptive mirrors are controlled by 672 electromagnetic actuators at a 1-kHz rate that in the first phase of the project will perform single-reference AO correction only. But when the NIRVANA module is placed on the LBT it will perform the ground layer loop. The MCAO system is designed according to the MFoV approach, as described in Subsection 2.B, with the stars in the external annular 6-arc-min FoV as references for the ground layer wave-front sensor and the stars in the 2-arc-min FoV as references for the high WFS. According to the optical design of the instrument, the NGS in the annular 6-arc-min FoV sees only the ground layer DM and does not use the corrections performed by the high DM. In the simulation code we define the telescope by taking into account the diameter of the primary mirror seen by the secondary and the 0.89-m-diameter central obstruction.

We take into account the minimum separation between the NGSs in the ground and in the high FoVs, respectively, of 25 and 20 arc sec. These separations are due to the dimensions occupied by the mechanical constraint. In the case we consider in the following simulations the central wavelength used for the wave-front sensing was the R band, whereas the results presented refer to the K band. We analyzed both the single channel and the interferometric modes. In the latter case we assumed that the piston correction residual has a rms value of $\lambda_p/4$, where λ_p is the scientific wavelength (K band), and a zero mean.

The star asterism studied in this simulation belongs to the faint range of magnitude for the low galactic latitudes. In fact, the probability of finding an asterism, in view of the LINC–NIRVANA con-

Table 8. Long-Exposure Data of the Cases Taken into Account for NIRVANA[a]

Case	Max SR	Average SR	rms SR	Peak to Valley
Single channel	0.21	0.13	0.03	0.30
Interferometric	0.13	0.12	0.002	0.004

[a]A differential piston error with standard deviation $\sigma_{\text{piston}} = \lambda/4$ is considered for the interferometric case. The results listed here refer to the 2-arc-min FoV for the single-channel case and to the central 20 arc sec × 20 arc sec for the interferometric case. In both cases Magnitude R integrated on a 2-arc-min FoV was 14.18.

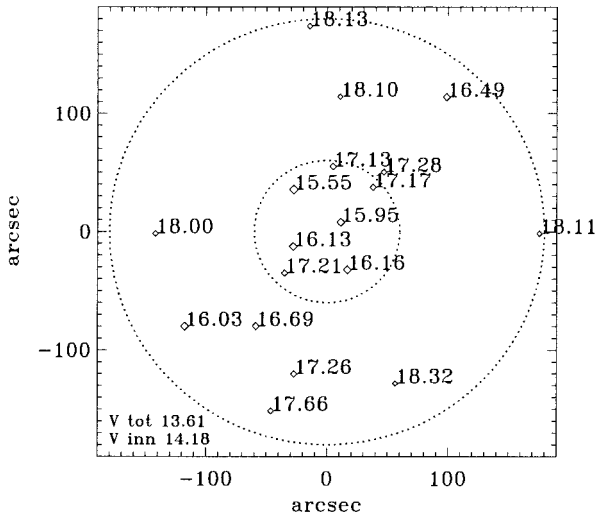

Fig. 12. Reference guide star positions and their magnitudes relative to the NIRVANA cases. The inner circle has a 2-arc-min FoV, with integrated R magnitude of 14.2; the larger circle has a 6-arc-min FoV, with total integrated magnitude of 13.6.

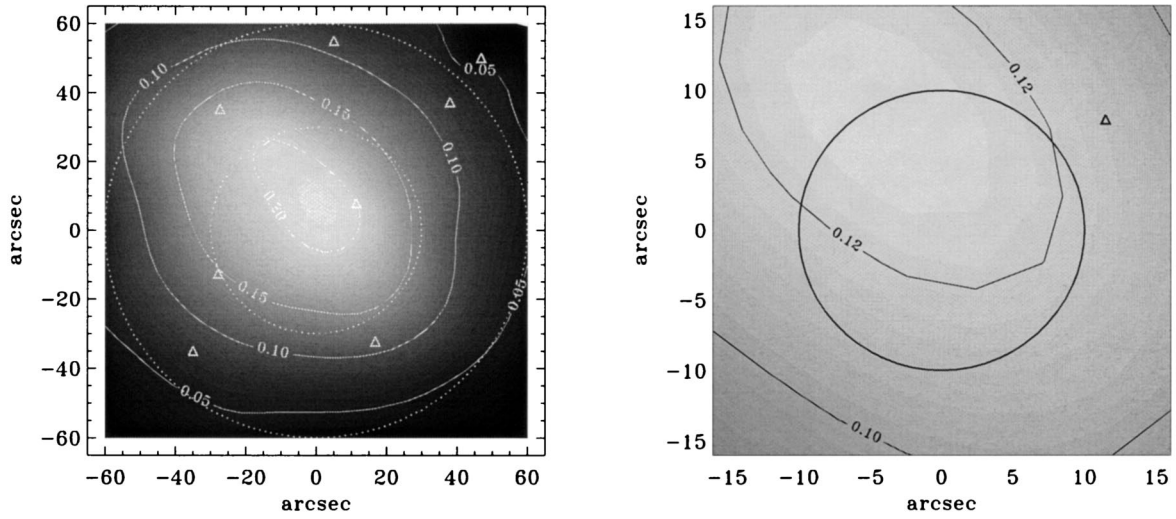

Fig. 13. Long-exposure SR maps obtained for a 2-arc-min FoV for left, a single channel and right, at 20 × 20 arcsec for the interferometric case. For both figures the same set of phase screens and the same system parameters listed in Table 7 were used.

straints on the minimum separation between the NGSs, that is brighter than the 14th integrated magnitude on the 6-arc-min FoV is more than 90%. This number decreases to 35% for the North galactic pole.[34] Figure 12 shows the results for both cases. For the single arm the full 2-arc-min corrected FoV is shown, where a significant SR of 0.21 was reached. In this case the correction shows a peak close to the center of the field because of the nonuniform NGS configuration: The correction is driven mainly by the brightest stars close to the on-axis direction. But this feature improves performance from the interferometric point of view, because for this option we considered a scientific camera centered on the on-axis direction with a FoV of 20 arc sec × 20 arc sec (Fig. 13). In this field the correction is quite uniform, and including also the piston-term error and the long-exposure SR (in this case the interferometric SR) is 0.12–0.13 (Table 8).

5. Conclusions

In this paper we have described the LOST simulation tool for multiconjugate layer-oriented systems. We validated all the main issues of the code by presenting the tests performed. These checks have shown that even if the LOST code does not compute the system performance in an end-to-end way, it gives results very similar to other end-to-end simulation codes (such as CAOS). This code can be a useful tool with which to evaluate the performance of the LO systems and to determine the system's parameters as the spatial and temporal samples that optimize the SR. Both the LO MAD and LINC–NIRVANA systems were analyzed by the LOST code, allowing us to estimate the instruments' performance and to optimize the AO parameters for the median atmosphere models considered. The authors will provide the source files for the code in response to an e-mail message from the reader.

We thank LINC–NIRVANA preliminary design review board members A. Glindemann, G. Herriot, N. Hubin, P. Lena, and F. Rigaut, to E. Fedrigo for useful discussions about the SH and pyramid WFS noise models, and to M. Le Louarn for the phase screen used in the MAD.

References

1. J. M. Beckers, "Detailed compensation of the isoplanatic patch size with multiconjugate adaptive optics," in *Proceedings of ESO Conference on Very Large Telescopes and Their Instrumentation*, M. H. Hulrich, ed. (European Southern Observatory, Garching, Germany, 1988), p. 693.
2. B. Ellerbroek, "First order performance evaluation of adaptive optics system for atmospheric turbulence compensation in an extended field-of-view astronomical telescope," J. Opt. Soc. Am. **11,** 783–805 (1994).
3. D. C. Johnston and B. M. Welsh, "Analysis of multiconjugate adaptive optics," J. Opt. Soc. Am. A **11,** 394–408 (1994).
4. H. W. Babcock, "The possibility of compensating astronomical seeing," Publ. Astron. Soc. Pac. **65,** 229–236 (1953).
5. R. Ragazzoni, "Adaptive optics for giants telescope: NGS vs. LGS," in *ESO Proceedings of the Backaskog Workshop on Extremely Large Telescopes*, T. Andersen, A. Ardeberg, and R. Gilmozzi, eds., Vol. 57 of ESO Conference and Workshop Proceedings (European Southern Observatory, Garching, Germany, 2000), pp. 175–180.
6. R. Ragazzoni, J. Farinato, and E. Marchetti, "Adaptive optics for 100-m-class telescopes: new challenges require new solutions," in *Adaptive Optical Systems Technology*, P. L. Wizinowich, ed., Proc. SPIE **4007,** 1076–1087 (2000).
7. J. Farinato, E. Fedrigo, E. Marchetti, and R. Ragazzoni, "More deformable mirrors (and higher Strehl) in layer-oriented for free," in *Beyond Conventional Adaptive Optics*, E. Vernet, R. Ragazzoni, N. Hubin, and S. Esposito, eds., Vol. 58 of ESO Conference and Workshop Proceedings (European Southern Observatory, Garching, Germany, 2002), pp. 91–99.
8. R. Ragazzoni, "Pupil plane wave front sensing with an oscillating prism," J. Mod. Opt. **43,** 289–293 (1996).
9. R. Ragazzoni and J. Farinato, "Sensitivity of a pyramidic wavefront sensor in closed loop adaptive optics," Astron. Astrophys. **350,** L23–L26 (1999).

10. J. B. Costa, R. Ragazzoni, A. Ghedina, M. Carbillet, C. Vrinaud, M. Feldt, S. Esposito, E. Puga, and J. Farinato, "Is there need of any modulation in the pyramid wavefront sensor?, in *Adaptive Optics System Technology II*, P. L. Wizinowich and D. Bonaccini, eds., Proc. SPIE **4839,** 288–298 (2003).
11. A. Ghedina, M. Cecconi, R. Ragazzoni, J. Farinato, A. Baruffolo, G. Crimi, E. Diolaiti, S. Esposito, L. Fini, M. Ghigo, E. Marchetti, T. Niero, and A. Puglisi, "On sky test of the pyramid wavefront sensor," in *Adaptive Optics System Technology II*, P. L. Wizinowich and D. Bonaccini, eds., Proc. SPIE **4839,** 869–877 (2003).
12. E. Diolaiti, R. Ragazzoni, and M. Tordi, "Closed loop performance of a layer-oriented multi-conjugate adaptive optics system," Astron. Astrophys. **372,** 710–718 (2001).
13. R. Ragazzoni, E. Diolaiti, J. Farinato, E. Jedrigo, E. Marchetti, M. Tordi, and Kirkmann, "Multiple field of view layer oriented adaptive optics," Astron. Astrophys. **396,** 731–744 (2002).
14. E. Fedrigo, E. Marchetti, E. Diolaiti, and C. Arcidiacono, "Layer-oriented single- and dual-field-of-view performance for a 100 m-class telescope," in *Future Giant Telescopes*, J. R. Angel and R. Gilmozzi, eds., Proc. SPIE **4840,** 415–426 (2003).
15. B. L. Ellerbroek, L. Gilles, and C. R. Vogel, "Numerical simulations of multiconjugate adaptive optics wave-front reconstruction on a giant telescope," Appl. Opt. **42,** 4811–4818 (2003).
16. M. Tordi, R. Ragazzoni, and E. Diolaiti, "Simulation of a layer-oriented MCAO system," in *Beyond Conventional Adaptive Optics*, E. Vernet, R. Ragazzoni, N. Hubin, and S. Esposito, eds., Vol. 58 of ESO Conference and Workshop Proceedings (European Southern Observatory, Garching, Germany, 2002), pp. 223–230.
17. N. Hubin, E. Marchetti, R. Conan, R. Ragazzoni, E. Diolaiti, M. Tordi, G. Rousset, T. Fusco, P. Y. Madec, D. Butler, and S. Esposito, "The ESO MCAO demonstrator: a European collaboration," in *Beyond Conventional Adaptive Optics*, E. Vernet, R. Ragazzoni, N. Hubin, and S. Esposito, eds., Vol. 58 of ESO Conference and Workshop Proceedings (European Southern Observatory, Garching, Germany, 2002), pp. 27–35.
18. R. Ragazzoni, T. M. Herbst, W. Gaessler, D. Andersen, C. Arcidiacono, A. Baruffolo, H. Baumeister, P. Bizenberger, E. Diolaiti, S. Esmosito, J. Farinato, H. W. Rix, R.-R. Rolhoff, A. Riccardi, P. Salinari, R. Soci, E. Vernet-Viard, and W. Xu, "A visible MCAO channel for NIRVANA at the LBT," in *Adaptive Optics System Technology II*, P. L. Wizinowich and D. Bonaccini, eds., Proc. Soc. Photo-Opt. Instrum. Eng. **4839,** 536–543 (2002).
19. J. N. Bahcall and M. Soneira, "The universe at faint magnitudes. I. Models for the galaxy and the predicted star counts," Astrophys. J. Suppl. Ser. **44,** 73–110 (1980).
20. I. Foppiani, C. Baffa, V. Biliotti, G. Bregoli, G. Cosentino, E. Giani, S. Esposito, B. Marano, and P. Salinari, "Photon counting CCDs as wavefront sensors for AO," in *Adaptive Optics System Technology II*, P. L. Wizinowich and D. Bonaccini, eds., Proc. SPIE **4839,** 312–316 (2003).
21. R. G. Lane, A. Glindemann, and J. C. Dainty, "Simulation of a Kolmogorov phase screen," Waves Random Media **2,** 209–224 (1992).
22. R. J. Noll, "Zernike polynomials and atmospheric turbulence," J. Opt. Soc. Am. **66,** 207–211 (1976).
23. J. Winker, "Effect of a finite outer scale on the Zernike decomposition of atmospheric turbulence," J. Opt. Soc. Am. A **8,** 1568–1573 (1991).
24. C. Vérinaud, C. Arcidiacono, M. Carbillet, E. Diolaiti, E. Vernet, R. Ragazzoni, and S. Esposito, "Layer oriented multiconjugate adaptive optics systems: performance analysis through extensive simulations," in *Adaptive Optics System Technology II*, P. L. Wizinowich and D. Bonaccini, eds., Proc. SPIE **4839,** 524–535 (2003).
25. G. Rousset, "Wave-front sensors," in *Adaptive Optics in Astronomy*, F. Roddier, ed. (Cambridge U. Press, New York, 1999), pp. 91–130.
26. S. Esposito and A. Riccardi, "Pyramid wavefront sensor behavior in partial correction adaptive optic systems," Astron. Astrophys. **369,** L9–L12 (1999).
27. T. Herbst, "Near infrared fringe-and-flexure tracker system," in *LINC-NIRVANA Preliminary Design Review Document* (Max Planck Institute for Astronomy, Heidelberg, Germany, 2003), pp. 123–137.
28. J. Beckers, "Adaptive optics for astronomy: principles, performance and applications," Annu. Rev. Astron. Astrophys. **31,** 13–62 (1993).
29. C. Arcidiacono, E. Diolaiti, R. Ragazzoni, E. Vernet, J. Farinato, and A. Baruffolo, "MAD layer-oriented WFS: system design analysis," in *MAD Final Design Review Document*, European Southern Observatory, ed., Tech. Rep. OWL-TRE-INA-60000-0064 (European Southern Observatory, Garching, Germany, 2002).
30. T. Herbst, "Performance simulations," in *LINC-NIRVANA Preliminary Design Review Document* (Max Planck Institute for Astronomy, Heidelberg, Germany, 2003), pp. 267–317.
31. F. Rigaut, B. L. Ellerbroek, and M. J. Northcott, "Comparison of curvature-based and Shack–Hartmann-based adaptive optics for the Gemini telescope," Appl. Opt. **36,** 2856–2868 (1997).
32. M. Carbillet, C. Vérinaud, B. Femenía, A. Riccardi, and L. Fini, "Simulation of astronomical adaptive optics systems. I. The software package CAOS," Astron. Astrophys, submitted for publication.
33. E. Vernet-Viard, R. Ragazzoni, C. Arcidiacono, A. Baruffolo, E. Diolaiti, J. Farinato, E. Fedrigo, E. Marchetti, R. Falomo, S. Esposito, M. Carbillet, and C. Vérinaud, "Layer-oriented wavefront sensor for MAD: status and progress," in *Adaptive Optics System Technology II*, P. L. Wizinowich and D. Bonaccini, eds., Proc. SPIE **4839,** 344–351 (2003).
34. C. Arcidiacono, E. Diolaiti, R. Ragazzoni, A. Baruffolo, A. Brindisi, J. Farinato, and E. Vernet, "Sky coverage and SR uniformity in layer-oriented MCAO," in *Astronomical Adaptive Optics Systems and Applications*, R. Tyson and M. Lloyd-Hart, eds., Proc. SPIE **5189,** 169–180 (2003).
35. J. M. Hill and P. Salinari, "Large binocular telescope project," in *Telescope Structures, Enclosures, Controls, Assembly/Integration/Validation, and Commissioning*, T. A. Sebring and T. Andersen, eds., Proc. SPIE **4004,** 36–46 (2000).
36. V. Gallieni, C. Del Vecchio, E. Anaclerio, and P. G. Lazzarini, "LBT adaptive secondary preliminary design," in *Adaptive Optical Systems Technology*, P. L. Wizinowich, ed., Proc. SPIE **4007,** 508–515 (2000).
37. R. Ragazzoni, E. Giallongo, F. Pasian, F. Pedichini, A. Fontana, G. Marconi, R. Speziali, M. Turatto, J. Danziger, G. Cremonese, R. Smareglia, D. Gallieni, E. Anaclerio, and P. G. Lazzarini, "Double prime focus camera for the $F/1.14$ Large Binocular Telescope," in *Optical and IR Telescope Instrumentation and Detectors*, I. Masanori and A. F. Moorwood, eds., Proc. SPIE **4008,** 439–446 (2000).
38. H. Mandel, I. Appenzeller, D. Bomans, F. Eisenhauer, B. Grimm, T. M. Herbst, R. Hofmann, M. Lehmitz, R. Lemke, M. Lehnert, R. Lenzen, T. Luks, R. Mohr, W. Seifert, N. A. Thatte, P. Weiser, and W. Xu, "LUCIFER: a NIR spectrograph and imager for the LBT," in *Optical and IR Telescope Instrumentation and Detectors*, I. Masanori and A. F. Moorwood, eds., Proc. SPIE **4008,** 767–777 (2000).
39. P. L. Byard and T. P. O'Brien, "MODS: optical design for a multi-object dual spectrograph," in *Optical and IR Telescope*

Instrumentation and Detectors, I. Masanori and A. F. Moorwood, eds., Proc. SPIE **4008,** 934–941 (2000).
40. P.-M. Hinz, J. R. Angel, D. W. McCarthy, W. F. Hoffman, and C. Y. Peng, "The large binocular telescope interferometer," in *Interferometry for Optical Astronomy II*, W. A. Traub, ed., Proc. SPIE **4838,** 108–112 (2003).
41. D. E. Groom, "Recent progress on CCDs for astronomical imaging," in *Optical and IR Telescope Instrumentation and Detectors*, I. Masanori and A. F. Moorwood, eds., Proc. SPIE **4008,** 634–645 (2000).
42. e2v Technologies, *CCD39–01 Back Illuminated High Performance CCD Sensor* (e2v Technologies, Chemlsford, UK, 2003).